

# Highly Strain-Tunable Interlayer Excitons in MoS<sub>2</sub>/WSe<sub>2</sub> Heterobilayers

Chullhee Cho,<sup>||</sup> Joeson Wong,<sup>||</sup> Amir Taqieddin, Souvik Biswas, Narayana R. Aluru, SungWoo Nam,<sup>\*</sup> and Harry A. Atwater<sup>\*</sup>



Cite This: <https://doi.org/10.1021/acs.nanolett.1c00724>



Read Online

ACCESS |



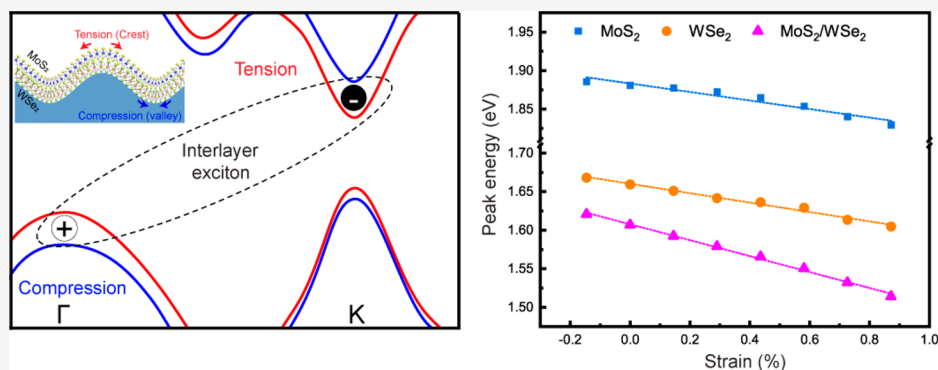
Metrics & More



Article Recommendations



Supporting Information



**ABSTRACT:** Interlayer excitons in heterobilayers of transition-metal dichalcogenides (TMDCs) have generated enormous interest due to their permanent vertical dipole moments and long lifetimes. However, the effects of mechanical strain on the optoelectronic properties of interlayer excitons in heterobilayers remain relatively uncharacterized. Here, we experimentally demonstrate strain tuning of  $\Gamma$ – $K$  interlayer excitons in molybdenum disulfide and tungsten diselenide (MoS<sub>2</sub>/WSe<sub>2</sub>) wrinkled heterobilayers and obtain a deformation potential constant of  $\sim 107$  meV/% uniaxial strain, which is approximately twice that of the intralayer excitons in the constituent monolayers. We further observe a nonmonotonic dependence of the interlayer exciton photoluminescence intensity with strain, which we interpret as being due to the sensitivity of the  $\Gamma$  point to band hybridization arising from the competition between in-plane strain and out-of-plane interlayer coupling. Strain engineering with interlayer excitons in TMDC heterobilayers offers higher strain tunability and new degrees of freedom compared to their monolayer counterparts.

**KEYWORDS:** heterostructure, interlayer exciton, strain, interlayer coupling, Poisson effect, deformation potential

Strain engineering of nanomaterials has received substantial interest because, as the physical length scales of nanomaterials become smaller, size effects enable fewer defects, such as grain boundaries, as well as diminishing bending rigidity, resulting in a superior yield strength with a highly elastic response compared to their bulk counterparts.<sup>1–3</sup> Two-dimensional (2D) materials are particularly suited for strain engineering because they combine a high in-plane mechanical strength and an extremely small bending rigidity with substantial strain tunability of electronic band structure.<sup>4–9</sup> The unique mechanical strength, flexibility, and tunability of 2D materials have therefore enabled their applications for wearable and flexible technologies<sup>10–12</sup> as well as fundamental studies of material properties under carefully engineered strain conditions. The semiconducting layered transition-metal dichalcogenides (TMDCs) have emerged as particularly interesting candidates for strain engineering, since they have exhibited exciton funneling,<sup>13–15</sup> strain-mediated phase tran-

sitions,<sup>16</sup> and the ability to form site-controlled quantum emitters via localized strains.<sup>17</sup>

Strain engineering has been explored in TMDC monolayers, multilayers, and heterostructures. Multilayer TMDCs are particularly interesting because they are known to exhibit interlayer exciton transitions, that is, optical transitions where the electron–hole pairs are located in different constituent layers bounded by strong Coulomb interaction.<sup>18</sup> These interlayer excitons have been observed to be strain tunable in homobilayers of molybdenum disulfide (MoS<sub>2</sub>)<sup>19,20</sup> and heterobilayers of molybdenum disulfide and tungsten diselenide (MoSe<sub>2</sub>/WSe<sub>2</sub>)<sup>21</sup> with deformation potentials of

**Received:** February 21, 2021

**Revised:** April 26, 2021

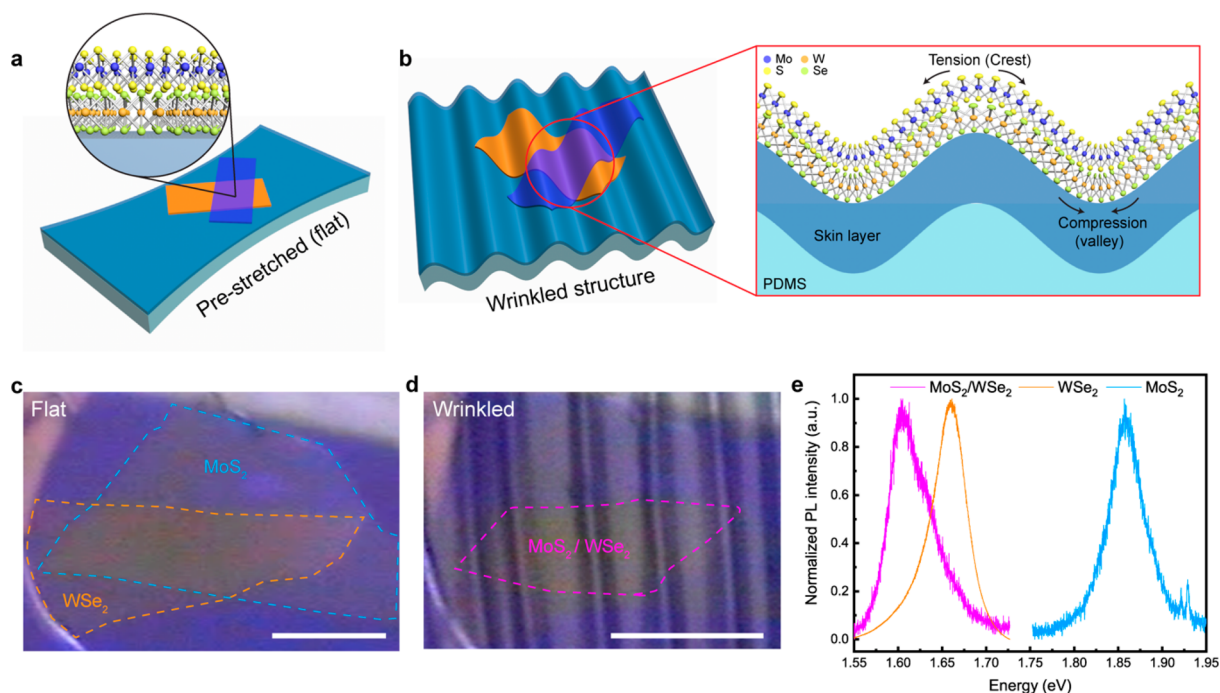


**Figure 1.** Fabrication of wrinkled  $\text{MoS}_2/\text{WSe}_2$  heterobilayer. (a) Schematic depiction of a vertical van der Waals heterobilayer on a prestretched elastomeric substrate. (b) After the release of the mechanically prestretched elastomeric substrate, a wrinkled heterostructure exhibiting a heterogeneous strain profile of alternating tension (at crest) and compression (at valley) is fabricated. (c) Optical microscopy image of a flat  $\text{MoS}_2/\text{WSe}_2$  heterobilayer with the estimated twist angle of  $50.7^\circ$ . Scale bar is  $10\ \mu\text{m}$ . (d) Optical microscopy image of a wrinkled  $\text{MoS}_2/\text{WSe}_2$  heterobilayer. Scale bar is  $10\ \mu\text{m}$ . (e) Photoluminescence spectra of flat monolayer  $\text{MoS}_2$ ,  $\text{WSe}_2$ , and  $\text{MoS}_2/\text{WSe}_2$ .

approximately 47 and 22 meV/%, respectively. Furthermore, other studies on multilayer structures have suggested that interlayer coupling should be an additional degree of freedom tunable via strain due to the Poisson effect,<sup>22,23</sup> but these effects on interlayer exciton transitions have yet to be observed.

In this work, we investigate the strain characteristics of momentum-space indirect  $\Gamma$ - $K$  interlayer exciton in a wrinkled molybdenum disulfide and tungsten diselenide ( $\text{MoS}_2/\text{WSe}_2$ ) heterobilayer. We spatially probed the effects of local strain in the wrinkled heterobilayer via photoluminescence (PL) and Raman measurements and found that the  $\Gamma$ - $K$  momentum-space indirect transition gives rise to a larger deformation potential (107 meV/%) compared to its intralayer counterpart because of the strain-sensitive orbital nature at the  $\Gamma$  point of the valence band and  $K$  point of the conduction band. Furthermore, we find that the interlayer exciton exhibits a nonmonotonic dependence in PL intensity with strain, which can be explained by a competition between the interlayer coupling and band structure modulation effects under strain. This hypothesis is supported by *ab initio* band structure calculations as well as Raman measurements, where we can directly measure the interlayer coupling.

For local strain engineering, we prepared wrinkled vertical heterostructures of  $\text{MoS}_2/\text{WSe}_2$  on an elastomeric substrate of poly(dimethylsiloxane) (PDMS) by using a combination of our heat-assisted PDMS-to-PDMS (PTP) assembly method and strain-release mechanism (see Methods and Figure S1 for more fabrication details). When a prestretched PDMS with the assembled heterobilayer of  $\text{MoS}_2/\text{WSe}_2$  via a PTP method (Figure 1a,c) is released, the heterobilayer deforms into a periodic wrinkled structure (Figure 1b) with a periodicity of  $\sim 4\ \mu\text{m}$  (Figure S1) as shown in an optical micrograph of the fabricated crumpled structure (Figure 1d). The periodic

wrinkled geometry induces a local stretching and compression of the heterobilayer lattice at the crests and valleys, respectively, resulting in a periodic local strain profile of alternating tensile and compressive strain within the TMDC heterostructure (Figure 1b).

To characterize the optical properties of the  $\text{MoS}_2/\text{WSe}_2$  heterobilayer, we performed steady-state PL spectroscopy and Raman spectroscopy under 532 nm excitation at room temperature over the fabricated  $\text{MoS}_2/\text{WSe}_2$  heterobilayer and adjacent isolated constituent monolayers before the release of the prestretch (flat state) (Figure 1e). We observed the intralayer emission at the exciton energies characteristic of  $\text{MoS}_2$  ( $\sim 1.88\ \text{eV}$  or 660 nm) and  $\text{WSe}_2$  ( $\sim 1.65\ \text{eV}$  or 750 nm) in adjacent isolated monolayers. In the heterobilayer, we observed a new PL emission peak red-shifted by  $\sim 75\ \text{meV}$  (or 30 nm) with respect to the intralayer A exciton of the  $\text{WSe}_2$  monolayer, which corresponds to a  $\Gamma$ - $K$  optical transition energy of  $\text{MoS}_2/\text{WSe}_2$ .<sup>24,25</sup> A confocal PL map (Figure S1) integrated over the two characteristic intralayer exciton peaks of  $\text{MoS}_2$  and  $\text{WSe}_2$  showed significant PL intensity quenching over the heterobilayer area, indicative of a rapid charge transfer due to the type-II nature of this interface. We further observed a uniform emission of the interlayer exciton at the  $\Gamma$ - $K$  optical transition energy of  $\text{MoS}_2/\text{WSe}_2$  across a relatively large area (Figure S2) as well as the out-of-plane Raman mode ( $A_{21g}^2$ ) of  $\text{WSe}_2$  at  $309\ \text{cm}^{-1}$  in our  $\text{MoS}_2/\text{WSe}_2$  heterobilayer (Figure S2), suggesting there is a strong interlayer coupling<sup>26</sup> between the  $\text{MoS}_2$  and  $\text{WSe}_2$  layers in the heterobilayer region.

To experimentally explore the effect of a local strain on the band structure and the resultant optical properties in terms of exciton emission, we first spatially resolved the PL energy shift of the intralayer and the interlayer excitons in the wrinkled monolayers and  $\text{MoS}_2/\text{WSe}_2$  heterobilayer (Figures 2 and S3).

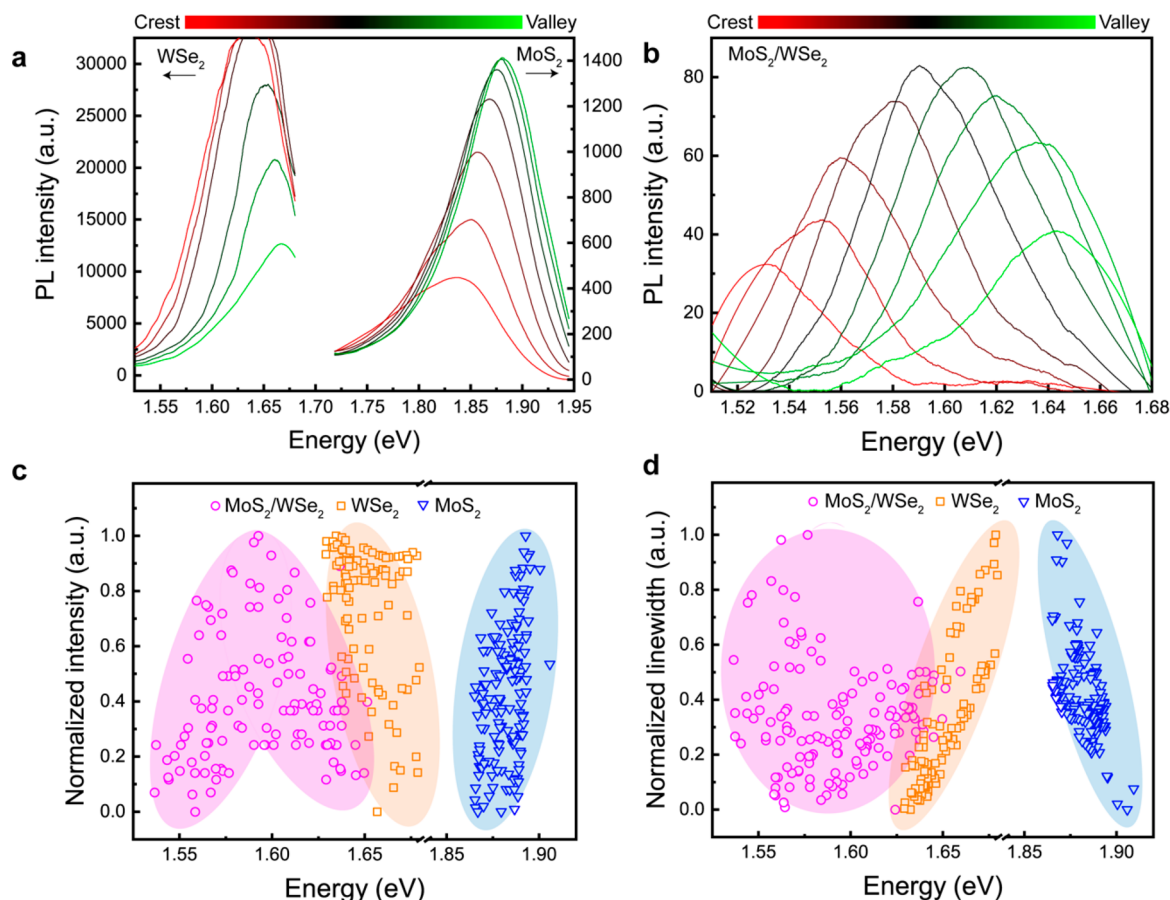


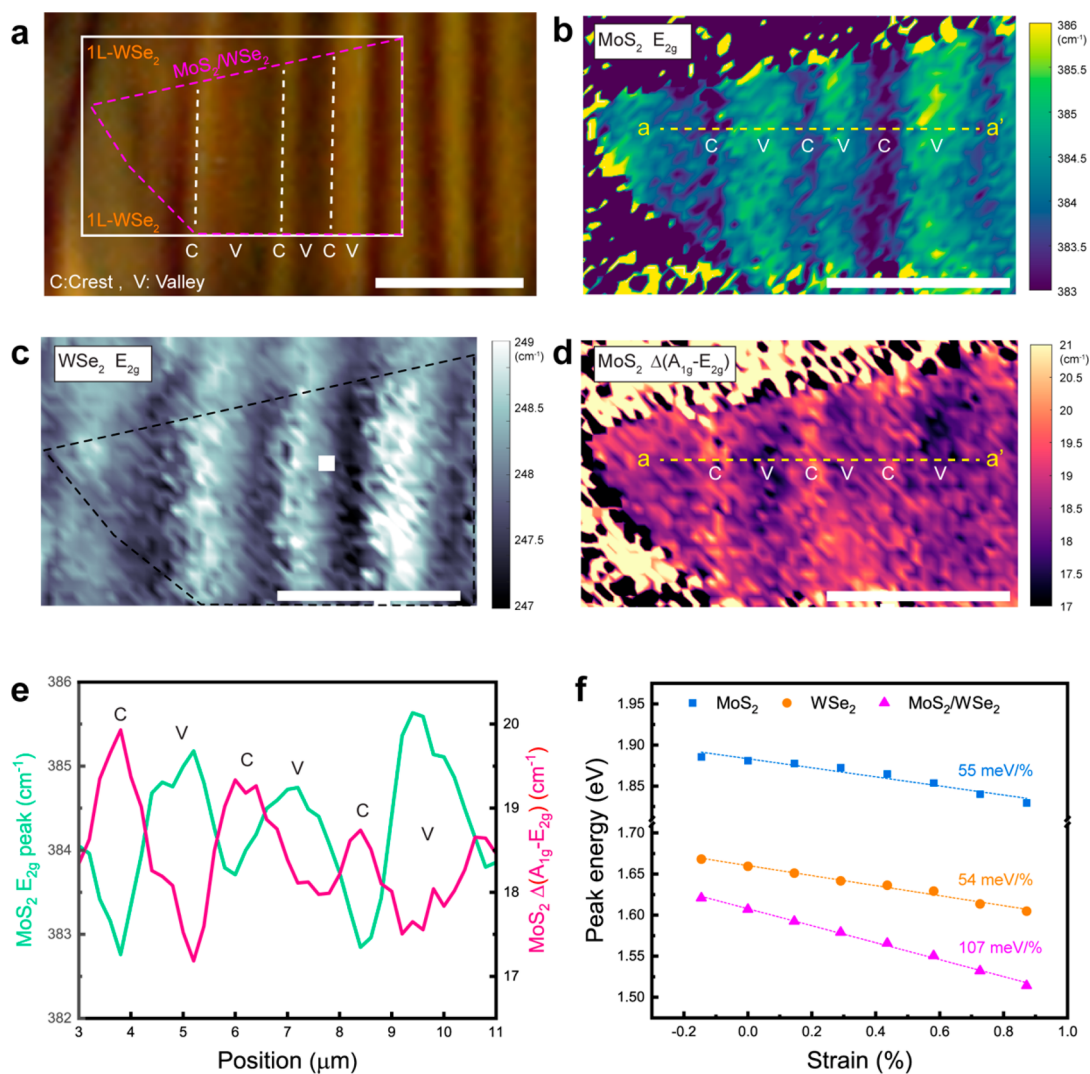
**Figure 2.** Photoluminescence of strained heterobilayers. Relative photoluminescence spectra (smoothed) of (a) WSe<sub>2</sub> and MoS<sub>2</sub> intralayer A excitons and (b) MoS<sub>2</sub>/WSe<sub>2</sub> interlayer exciton over a representative wrinkle (from the valley to the crest). The monolayer WSe<sub>2</sub> luminescence saturated the detector in these mapping measurements, creating a top-hat effect in the spectra. Scatter plots over multiple wrinkles that show how the (c) normalized intensity and (d) line width of WSe<sub>2</sub>, MoS<sub>2</sub>, and MoS<sub>2</sub>/WSe<sub>2</sub> vary with exciton energy. Each point refers to a separate spectrum measured and fitted to a Gaussian function, over the relevant region of the sample.

Typical PL spectra measured at room temperature across a single-wrinkle profile are shown in Figure 2a for the intralayer excitons of WSe<sub>2</sub> and MoS<sub>2</sub> and in Figure 2b for the interlayer exciton of the MoS<sub>2</sub>/WSe<sub>2</sub> heterobilayer. In both cases, we observed a gradual shift of the emission peak energy along with the wrinkle profile and observed that the energy peak shifts within the structure can be modulated up to  $\sim 107$  meV for the interlayer exciton, compared to  $\sim 54$  meV for WSe<sub>2</sub> and 55 meV for MoS<sub>2</sub> intralayer excitons under uniaxial deformation. We observed a greater tunability of the peak energy shifts in the interlayer exciton than in the intralayer excitons. We further observed the peak energies red-shifted (blue-shifted) at the crest (valley) of the wrinkled structure relative to the peak energies in the flat state for both intralayer and interlayer excitons. These observations are indicative of both tensile (local stretching of atomic lattices at the crests) and compressive (at the valleys) strain applied via our fabricated wrinkled structure, which suggests a band structure modulation via local strain profile.<sup>27</sup> The observation of luminescence peak energy shifts along the wrinkle profile allows us to correlate the spatial position with a locally applied strain.

We also observed strikingly different qualitative trends for the variation of PL intensity with strain between the intralayer and interlayer excitons for our wrinkled structure. Specifically, we observed that the PL intensity of the WSe<sub>2</sub> (MoS<sub>2</sub>) intralayer exciton was highest (lowest) at the crests and lowest

(highest) at the valleys. Thus, the PL intensity of WSe<sub>2</sub> (MoS<sub>2</sub>) monotonically increases (decreases) with increasing tensile strain (Figure 2a). In contrast, the maximum peak intensity of the interlayer exciton in the heterobilayer region occurs at an intermediate position between the crest and valley, with a peak energy of  $\sim 1.6$  eV. By comparing this peak energy with the flat-state peak energy, we find that the maximum peak intensity of the interlayer exciton occurs when the heterobilayer is under a mild compression. Thus, by examining the relationship between the peak energy with the peak intensity, we find that the MoS<sub>2</sub>/WSe<sub>2</sub> interlayer exciton PL intensity is nonmonotonic with local strain. In other words, the interlayer exciton PL intensity appears to decrease with both increasing tensile and compressive strain, which is in direct contrast to the monotonic peak intensity versus peak energy behavior observed for intralayer monolayer emission.

To substantiate our findings, we show scatter plots between the peak intensity versus peak energy (Figure 2c), where each point corresponds to an individually fitted spectrum with the peak intensities normalized to the brightest spot within that region of the sample. We observed this nonmonotonic interlayer exciton intensity trend across multiple spots throughout the entire sample. We also found that this interlayer exciton intensity trend also appears in various other samples we measured (see Figure S4) as well as when we account for the finite depth of focus in our measurements (see



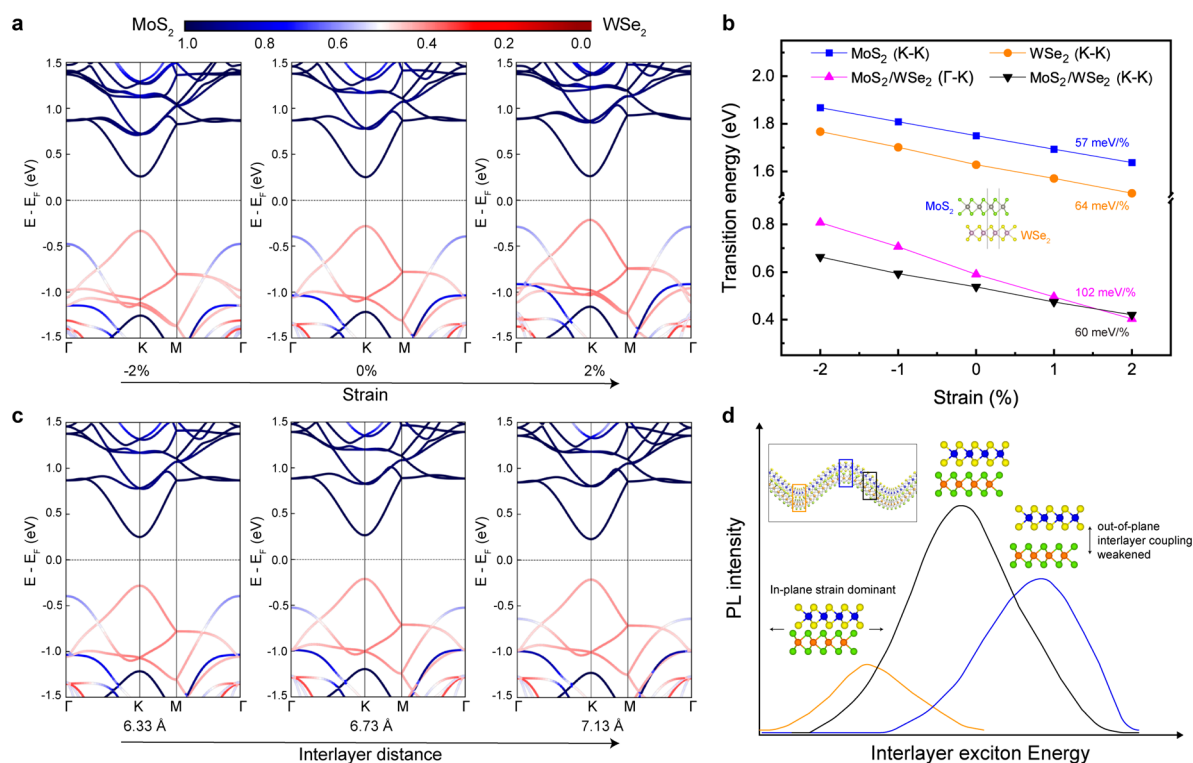
**Figure 3.** Raman spectroscopy and deformation potentials of strained heterobilayers. (a) An optical microscopy image of the wrinkled  $\text{MoS}_2/\text{WSe}_2$  heterobilayer. Vertical dotted white lines indicate crests of wrinkles. Magenta dotted lines indicate the boundary between adjacent monolayer  $\text{WSe}_2$  and heterobilayer of  $\text{MoS}_2/\text{WSe}_2$  areas. Spatially resolved Raman mapping of (b)  $\text{MoS}_2 E_{2g}$  mode and (c)  $\text{WSe}_2 E_{2g}$  mode peak positions. (d) Peak position separation between  $\text{MoS}_2 A_{1g}$  and  $E_{2g}$  modes ( $A_{1g}-E_{2g}$ ). All the scale bars are  $5 \mu\text{m}$ . (e) Raman peak shifts of  $\text{MoS}_2 E_{2g}$  and  $A_{1g}-E_{2g}$  modes as a function of position along the  $a-a'$  line indicated in (b, d). C and V are the crests and valleys of the wrinkle, respectively. (f) Experimentally derived deformational potentials of  $\text{MoS}_2$  and  $\text{WSe}_2$  intralayer excitons, and  $\text{MoS}_2/\text{WSe}_2$  interlayer exciton obtained from measured Raman and PL spectra. Dashed lines correspond to linear fits of the deformation potential curve.

Figure S5). Exciton funneling effects are not a dominant effect, since we did not observe the highest intensity at the lowest energy of emission in our heterobilayers.

To gain additional insight on the mechanism of intensity modulation, we show similar scatter plots in Figure 2d between the fitted peak line width (full width at half-maximum) and peak energy. Interestingly, while the interlayer exciton shows no obvious correlation between the peak line width and peak energy, the  $\text{WSe}_2$  and  $\text{MoS}_2$  intralayer excitons show a clear behavior of positive and negative correlation, respectively. Moreover, these trends in line width contrast with the trends in intensity for the individual monolayers; that is, peak intensity and line width are apparently inversely correlated, which can be observed more clearly in Figure 2a of the individual spectra. By correlating the peak energy shift to an applied strain, the  $\text{WSe}_2$  ( $\text{MoS}_2$ ) peak line width decreases (increases) with an applied tensile strain. Similarly, the  $\text{WSe}_2$  ( $\text{MoS}_2$ ) peak intensity increases (decreases) with an applied tensile strain.

These effects of strain on the PL intensity and line width of the individual monolayers are well-established<sup>7–9,28,29</sup> and can be explained by the decreased (increased) scattering to the neighboring Q ( $\Gamma$ ) valley in the  $\text{WSe}_2$  ( $\text{MoS}_2$ ) conduction (valence) band from the K point. In other words, interband transitions in  $\text{WSe}_2$  ( $\text{MoS}_2$ ) become effectively more direct (indirect) as a tensile strain is applied. In contrast to the intralayer excitons, the lack of line width modulation with local strain in interlayer exciton emission suggests that there is little modulation of the nonradiative scattering channels.

To better understand the cause of the nonmonotonic intensity variation for the interlayer exciton, we turn to Raman spectroscopy measurements for additional insight as to the mechanisms that may be at play, that is, investigating the in-plane and out-of-plane strain resulting from topological deformation of the wrinkled heterobilayer (Figure 3a). We show that the Raman characteristics of the  $\text{MoS}_2 E_{2g}$  (Figure 3b) and  $\text{WSe}_2 E_{2g}$  (Figure 3c) modes<sup>30–32</sup> are well-modulated



**Figure 4.** DFT calculation of strained MoS<sub>2</sub>/WSe<sub>2</sub> heterobilayers. (a) The band structure of MoS<sub>2</sub>/WSe<sub>2</sub> heterobilayers under different in-plane strain values with AB stacking. The color scale describes the origin of the electronic states where the purely blue (red) are completely localized electronic states that come from the MoS<sub>2</sub> (WSe<sub>2</sub>) layer, and intermediate colors have electronic states that are delocalized across both layers (i.e., hybridized state that come from both MoS<sub>2</sub> and WSe<sub>2</sub> layers). (b) Electronic transition energy for *K*–*K* transitions of monolayer MoS<sub>2</sub> and monolayer WSe<sub>2</sub>,  $\Gamma$ –*K* transition of MoS<sub>2</sub>/WSe<sub>2</sub>, and the *K*–*K* transition of MoS<sub>2</sub>/WSe<sub>2</sub>, as a function of strain. The inset schematic depicts the AB stacking order. (c) The band structure of MoS<sub>2</sub>/WSe<sub>2</sub> heterobilayers as a function of interlayer distance. (d) Schematic depiction of the nonmonotonic behavior of the interlayer exciton PL intensity due to the competition between in-plane strain and out-of-plane interlayer coupling.

by our wrinkled sample profile, where the peaks are red-shifted (blue-shifted) at the crest (valley), which corresponds well with the topographical features seen in the optical micrograph as shown in Figure 3a. Because the  $E_{2g}$  mode is an in-plane vibrational mode, it is therefore sensitive to in-plane strain. However, we did not use the WSe<sub>2</sub>  $E_{2g}$  mode for a quantitative measure of in-plane strain because of the degeneracy between the WSe<sub>2</sub>  $E_{2g}$  and  $A_{1g}$  modes. We conclude that there is a uniform and controlled tension (compression) at the crest (valley) with our wrinkled geometry, which corroborates our observations in PL spectroscopy measurements.

To study the effects of local strain on the interlayer coupling in the heterobilayer, we examined the mode separation between the MoS<sub>2</sub>  $E_{2g}$  (in-plane) and  $A_{1g}$  (out-of-plane) modes. The wavenumber separation between  $A_{1g}$  and  $E_{2g}$  has been used as a quantitative measure of the interlayer mechanical coupling strength in artificially stacked bilayers, where a larger peak separation is indicative of a stronger interlayer coupling.<sup>33,34</sup> The mode separation has also been used as an effective proxy for the number of layers in naturally exfoliated MoS<sub>2</sub>, that is,  $\sim 19$  cm<sup>-1</sup> for monolayer and  $\sim 21$  cm<sup>-1</sup> for bilayer MoS<sub>2</sub>.<sup>35,36</sup> We show the map of the wavenumber separation between the MoS<sub>2</sub>  $A_{1g}$  and  $E_{2g}$  modes,  $\Delta(A_{1g} - E_{2g})$  in Figure 3d. In our strained heterobilayer, we observed the  $A_{1g}$  and  $E_{2g}$  mode separation changes from a value of  $\sim 20$  cm<sup>-1</sup> at the crest to  $\sim 17$  cm<sup>-1</sup> at the valley (Figure 3e). We also observed a modulation of the integrated intensity ratio ( $A_{1g}/E_{2g}$ ) at the crest and valley (Figure S6), which is comparable to the ratio observed

between a naturally exfoliated bilayer and a monolayer of MoS<sub>2</sub>.<sup>37</sup> Therefore, we conclude that the modulation of the  $E_{2g}$  mode together with the  $A_{1g}$  mode along the wrinkle profile suggests the interlayer coupling in the heterobilayer is tuned between a stronger interlayer coupling (larger  $\Delta$ ) and a weaker interlayer coupling (smaller  $\Delta$ ) at different locations of the wrinkled heterobilayer. We then postulate that, in our wrinkled strain profile of the heterobilayer, we are observing a simultaneous modulation of the interlayer coupling between MoS<sub>2</sub> and WSe<sub>2</sub> as well as in-plane strain in the heterobilayer. Specifically, there appears to be a stronger interlayer coupling at the crests, which are in tension, as compared to at the valleys, which are in compression. This trend is highlighted by the linecut in Figure 3e. Thus, the combination of these two effects—in-plane strain and out-of-plane interlayer coupling in our wrinkled structure—are hypothesized to result in the nonmonotonic intensity profile of the interlayer exciton observed in Figure 2.

Together with the Grüneisen parameters of the  $E_{2g}$  Raman modes<sup>29–32</sup> and the PL peak shifts observed earlier, we can also extract an experimental deformation potential for our system, which yields values of  $\sim 55$  meV/% for MoS<sub>2</sub>, 54 meV/% for WSe<sub>2</sub>, and 107 meV/% for the  $\Gamma$ –*K* transition interlayer exciton under a uniaxial strain (Figure 3f). The estimated strain values from the Raman modes corroborate well with those estimated from the surface morphology (see Figure S7 and the Supplementary Note in the Supporting Information). The deformation potentials of the intralayer excitons also correspond well with reported values,<sup>28,29</sup> and the interlayer

exciton deformation potential is notably almost twice that of the intralayer excitons.

To investigate whether the experimental observations described earlier are consistent with *ab initio* calculations, we examine the electronic band structure of the strained heterobilayer by performing density functional theory (DFT) calculations using the Perdew–Burke–Ernzerhof (PBE) functional<sup>38</sup> (see Methods for more details). Although the PBE functional underestimates the absolute value of the bandgap for TMDC monolayers, it has shown the ability to predict accurate deformation potential constants that match with the experimental measurements and the high-level simulations using the coupled GW and Bethe–Salpeter equations (BSE) approach.<sup>15,39</sup> We coupled PBE with D3 corrections to capture accurate van der Waals (vdW) interactions in the layered materials.<sup>40,41</sup>

The band structure under different strain conditions is shown in Figure 4a for AB stacking, where we project the weighted orbital contributions onto either of the constitutive layers. As noted previously, the interlayer exciton energetic transition we observe is presumed to be the  $\Gamma$ – $K$  transition, because the MoS<sub>2</sub> and WSe<sub>2</sub> layers are not intentionally aligned to their crystallographic axes, and therefore the effective oscillator strength of the  $K$ – $K$  transition would be substantially weaker.<sup>24</sup> We further observe that the theoretically calculated deformation potential (Figure 4b) for the  $\Gamma$ – $K$  transition provides a much closer match to the experimentally observed value (Figure 3f), compared to the  $K$ – $K$  transition. The increased deformation potential constant comes from the fact that the nature of the wave functions at the  $\Gamma$  point (valence band) and  $K$  point (conduction band) are of a similar orbital nature (specifically, the  $d_{z^2}$  orbital)<sup>42</sup> and is therefore affected in a similar way under a mechanical strain. We also find that the  $\Gamma$  point is particularly sensitive to interlayer coupling and band hybridization, as observed previously<sup>43–45</sup> (Figure S8). Lastly, we remark that this  $\Gamma$ – $K$  interlayer exciton is MoS<sub>2</sub>-like in character and has strain characteristics akin to a natural bilayer of MoS<sub>2</sub>, where the  $\Gamma$ – $K$  indirect transition of a natural MoS<sub>2</sub> bilayer was also observed to have a higher deformation potential compared to the direct  $K$ – $K$  transition and a decreasing PL intensity under a tensile strain.<sup>29</sup>

The band structure calculations also enable us to understand the effects of strain on the band hybridization and therefore the PL intensity trends of the interlayer exciton observed in Figure 2. Specifically, we presume that the oscillator strength ( $\sigma_k$ ) of this interlayer exciton transition is proportional to the MoS<sub>2</sub> character ( $\zeta$ ) at the  $\Gamma$  point;<sup>24</sup> that is,  $\sigma_k \sim \zeta = |\langle \text{MoS}_2 | \Gamma \rangle|^2$ . Therefore, by assuming the oscillator strength scales with the MoS<sub>2</sub> character at the  $\Gamma$  point, that is,  $\Delta\sigma_k/\sigma_{k,0} \approx \Delta\zeta/\zeta_0$ , we can calculate relative oscillator strength modulations by examining the band structure wave function projections (weighted orbital contributions). The calculations show an increase of band hybridization (less MoS<sub>2</sub> contribution) with tensile strain (Figure 4a). The relative modulation in  $\zeta$  would be ca.  $-0.02/\%$  with strain (Figure S9), where the negative sign signifies a decrease in  $\zeta$  with tensile strain. Similarly, we performed calculations of the band structure as a function of interlayer spacing (Figure 4c) and found an increase in band hybridization with an increased interlayer distance. We calculate the relative modulation in  $\zeta$  to be ca.  $-0.13/\text{\AA}$  with interlayer distance (Figure S9). Thus, we predict that the relative oscillator strength and therefore the PL intensity would

decrease with both tensile strain and increased interlayer distance.

Our theoretical calculations corroborate well with the experimental trends of PL intensity observed for the interlayer exciton if we hypothesize that, (1) as tensile strain is applied, the interlayer coupling is sufficiently strong so that the in-plane tensile strain reduces the PL intensity due to the decrease in the oscillator strength and (2) as compressive strain is applied, the out-of-plane interlayer coupling is weakened, so that the PL intensity also decreases due to the substantially reduced oscillator strength. Therefore, the PL intensity would likely be maximized near the zero-strain configuration, as we observed experimentally. These effects are depicted schematically in Figure 4d and suggest that multilayer and heterobilayer TMDCs may exhibit a positive Poisson effect, where the reduced out-of-plane interlayer coupling is always accompanied by compressive in-plane strain and vice versa. The calculated effects of larger strain values, other interlayer spacings, and different stacking configurations on the electronic band structure are also shown in Figure S10, and we find that the description given above is of generally applicability for this relatively twist-angle insensitive MoS<sub>2</sub>/WSe<sub>2</sub> heterobilayer.<sup>24,25</sup>

In summary, our findings suggest that interlayer excitons in transition-metal dichalcogenide heterobilayers are particularly attractive for strain engineering. Specifically, we found that momentum-space indirect  $\Gamma$ – $K$  interlayer excitons in MoS<sub>2</sub>/WSe<sub>2</sub> heterobilayers have a deformation potential of approximately twice that of the constituent intralayer excitons. In addition, we observed that the interlayer coupling of the heterobilayer can be directly tuned in our locally strained structures. We showed that the simultaneous modulation of the out-of-plane interlayer coupling and the in-plane strain in our wrinkled structures can explain the nonmonotonic dependence of the interlayer exciton PL peak intensity with peak energy. More generally, the possibility of coupling between in-plane and out-of-plane effects in multilayered structures, akin to a Poisson effect, should be considered when strain engineering layered 2D materials. The existence of multiple knobs that strain can tune in the interlayer exciton system highlights the potential and promise for the next generation of interlayer exciton strain-based devices.

## METHODS

### Sample Preparation Via the PTP Assembly Process.

Wrinkled vdW heterostructures were fabricated via a combination of PTP assembly process and strain-release mechanism using a stretchable substrate of PDMS. As the first step of the PTP dry assembly process, a monolayer of WSe<sub>2</sub> (HQ Graphene) is exfoliated directly on a uniaxially prestretched PDMS substrate ( $\sim 120\%$ ) with a skin layer, which was formed by an O<sub>2</sub> plasma treatment (Figure S1). This stiff skin layer on the PDMS is used to guide conformal out-of-plane deformation (i.e., wrinkling) of the transferred vdW heterobilayer when the substrate is contracted after the release of the prestretched PDMS. The stiff skin layer enables an increased transfer of strain by reducing the Young's modulus mismatch between the PDMS and the TMDC heterobilayer.<sup>46</sup> Next, a monolayer of MoS<sub>2</sub> (HQ Graphene) is mechanically exfoliated directly on a separate PDMS substrate. Then the exfoliated monolayer MoS<sub>2</sub>/PDMS directly transfers onto the monolayer WSe<sub>2</sub>/PDMS via a gentle, heat-assisted ( $\sim 70$  °C) PTP transfer stamping (Figure S1), forming a

vertically stacked heterostructure (Figure S2). Target-exfoliated monolayers can be integrated into a heterostructure without contacting any other materials that are essential for avoiding lithographic or etching process-induced polymeric or solvent residues. We note that our PTP assembly process works with either commercially available PDMS slabs (e.g., Gel-Pak) or homemade PDMS (Dow Inc. Sylgard) substrates. A mechanical contraction after the release of the prestretched PDMS resulted in a periodic wrinkled heterobilayer. We note that the assembled heterobilayer was constrained by a poly(methyl methacrylate) (PMMA) capping layer, which acts as a clamp to prevent slippage of the heterobilayer when it conforms to the underlying PDMS layer.

**Electronic Structure Calculations.** We performed *ab initio* DFT calculations for the different MoS<sub>2</sub> and WSe<sub>2</sub> monolayers and MoS<sub>2</sub>/WSe<sub>2</sub> stackings using the Vienna Ab initio simulation package (VASP) to compute the atomic electronic structures.<sup>47</sup> The PBE exchange-correlation functional was applied.<sup>38</sup> We used D3 corrections for van der Waals interactions.<sup>40,41</sup> We considered the ground-state band structure as an approximate description for the optical transitions in the MoS<sub>2</sub>/WSe<sub>2</sub> heterobilayer. The ultrasoft pseudopotentials were used with a 450 eV energy cutoff in all simulations. The structure relaxation was performed using Gamma-point-centered k-point of 4 × 4 × 1. All structures were fully relaxed, until the force on each atom reached less than 0.01 eV/Å and the total energy was converged within 10<sup>-6</sup> eV. Each unit cell consisted of 12 atoms of MoS<sub>2</sub> as a monolayer or 12 atoms of WSe<sub>2</sub> as a monolayer or both for the MoS<sub>2</sub>/WSe<sub>2</sub> stacking. During the relaxation of the MoS<sub>2</sub>/WSe<sub>2</sub> stacking structure, the volume of the unit cell was kept variable to determine the optimized lattice constant and to reduce the mismatch between the MoS<sub>2</sub> and WSe<sub>2</sub> allowing determination of the unstrained structure. In all simulations, the vacuum is kept at least 15 Å to avoid spurious interactions in the aperiodic direction. Once the structures were fully relaxed and the unstrained configurations were determined, we applied strain in one of the periodic directions. After all the relaxed configurations of the unstrained and strained structures were obtained, the band structures were computed using a total of 90 K-points in the G-K-M-G path.

## ■ ASSOCIATED CONTENT

### SI Supporting Information

The Supporting Information is available free of charge at <https://pubs.acs.org/doi/10.1021/acs.nanolett.1c00724>.

PDMS-to-PDMS transfer; additional band structure calculations under different stacking configurations, larger strain values and twist angles; additional experimental data (PDF)

## ■ AUTHOR INFORMATION

### Corresponding Authors

**SungWoo Nam** – Department of Mechanical Science and Engineering and Department of Materials Science and Engineering, University of Illinois at Urbana–Champaign, Urbana, Illinois 61801, United States; [orcid.org/0000-0002-9719-7203](https://orcid.org/0000-0002-9719-7203); Email: [swnam@illinois.edu](mailto:swnam@illinois.edu)

**Harry A. Atwater** – Department of Applied Physics and Materials Science, California Institute of Technology, Pasadena, California 91125, United States; [orcid.org/0000-0001-9435-0201](https://orcid.org/0000-0001-9435-0201); Email: [haa@caltech.edu](mailto:haa@caltech.edu)

## Authors

**Chullhee Cho** – Department of Mechanical Science and Engineering, University of Illinois at Urbana–Champaign, Urbana, Illinois 61801, United States; [orcid.org/0000-0002-9624-8072](https://orcid.org/0000-0002-9624-8072)

**Jeoson Wong** – Department of Applied Physics and Materials Science, California Institute of Technology, Pasadena, California 91125, United States; [orcid.org/0000-0002-6304-7602](https://orcid.org/0000-0002-6304-7602)

**Amir Taqieddin** – Department of Mechanical Science and Engineering, University of Illinois at Urbana–Champaign, Urbana, Illinois 61801, United States; [orcid.org/0000-0002-5743-7110](https://orcid.org/0000-0002-5743-7110)

**Souvik Biswas** – Department of Applied Physics and Materials Science, California Institute of Technology, Pasadena, California 91125, United States

**Narayana R. Aluru** – Department of Mechanical Science and Engineering, University of Illinois at Urbana–Champaign, Urbana, Illinois 61801, United States; [orcid.org/0000-0002-9622-7837](https://orcid.org/0000-0002-9622-7837)

Complete contact information is available at:

<https://pubs.acs.org/10.1021/acs.nanolett.1c00724>

## Author Contributions

<sup>||</sup>These authors contributed equally. C.C., J.W., S.N., and H.A.A. developed the ideas. C.C. and J.W. fabricated the samples and performed the measurements, with assistance from S.B. The first-principles simulations were performed by A.T. under the supervision of N.R.A. The manuscript was written by C.C. and J.W., with input from all authors. All authors contributed to the discussion and interpretation of results, as well as the presentation and preparation of the manuscript.

## Notes

The authors declare no competing financial interest.

## ■ ACKNOWLEDGMENTS

This work was primarily supported by the “Photonics at Thermodynamic Limits” Energy Frontier Research Center funded by the U.S. Department of Energy, Office of Science, Office of Basic Energy Sciences under Award No. DE-SC0019140, which supported the strained interlayer exciton sample fabrication and experimental optical measurements. C.C. also acknowledges additional support from the NASA Space Technology Research Fellow Grant No. 80NSSC17K0149, and J.W. acknowledges additional support from a National Science Foundation (NSF) Graduate Research Fellowship under Grant No. 1144469. S.N. gratefully acknowledges support from the AFOSR (FA2386-17-1-4071), NSF (MRSEC DMR-1720633 and CMMI-1554019), and ONR YIP (N00014-17-1-2830), which supported additional wrinkled heterobilayer sample fabrication and optical measurements. The density functional theory calculations performed by A.T. and N.R.A. acknowledge support from the NSF (MRSEC DMR-1720633 and CMMI-1921578), ONR (Grant No. N00014-19-1-2596), and the supercomputing resources provided by the Extreme Science and Engineering Discovery Environment (XSEDE) (supported by NSF Grant No. OCI1053575), Blue Waters (supported by NSF Award Nos. OCI-0725070 and ACI-1238993 and the state of Illinois, and as of December, 2019, supported by the National Geospatial-Intelligence Agency), and Frontera computing project at the

Texas Advanced Computing Center (supported by NSF Grant No. OAC-1818253). C.C. acknowledges Dr. J. S. Lopez who assisted the X-ray reflectometry analysis.

## REFERENCES

- (1) Griffith, A. A. The Phenomena of Rupture and Flow in Solids. *Philos. Trans. R. Soc. London Ser. A* **1921**, *221*, 163.
- (2) Greer, J. R.; Nix, W. D. Nanoscale Gold Pillars Strengthened through Dislocation Starvation. *Phys. Rev. B: Condens. Matter Mater. Phys.* **2006**, *73* (24), 1–6.
- (3) Zhu, T.; Li, J. Ultra-Strength Materials. *Prog. Mater. Sci.* **2010**, *55* (7), 710–757.
- (4) Lee, C.; Wei, X.; Kysar, J. W.; Hone, J. Measurement of the Elastic Properties and Intrinsic Strength of Monolayer Graphene. *Science* **2008**, *321*, 385–388.
- (5) Zhan, H.; Guo, D.; Xie, G. X. Two-Dimensional Layered Materials: From Mechanical and Coupling Properties towards Applications in Electronics. *Nanoscale* **2019**, *11* (28), 13181–13212.
- (6) Peng, Z.; Chen, X.; Fan, Y.; Srolovitz, D. J.; Lei, D. Strain Engineering of 2D Semiconductors and Graphene: From Strain Fields to Band-Structure Tuning and Photonic Applications. *Light: Sci. Appl.* **2020**, *9* (1). DOI: 10.1038/s41377-020-00421-5.
- (7) Desai, S. B.; Seol, G.; Kang, J. S.; Fang, H.; Battaglia, C.; Kapadia, R.; Ager, J. W.; Guo, J.; Javey, A. Strain-Induced Indirect to Direct Bandgap Transition in Multilayer WSe<sub>2</sub>. *Nano Lett.* **2014**, *14* (8), 4592–4597.
- (8) Lloyd, D.; Liu, X.; Christopher, J. W.; Cantley, L.; Wadehra, A.; Kim, B. L.; Goldberg, B. B.; Swan, A. K.; Bunch, J. S. Band Gap Engineering with Ultralarge Biaxial Strains in Suspended Monolayer MoS<sub>2</sub>. *Nano Lett.* **2016**, *16* (9), 5836–5841.
- (9) Niehues, I.; Schmidt, R.; Drüppel, M.; Maruhn, P.; Christiansen, D.; Selig, M.; Berghäuser, G.; Wigger, D.; Schneider, R.; Braasch, L.; Koch, R.; Castellanos-Gomez, A.; Kuhn, T.; Knorr, A.; Malic, E.; Rohlfing, M.; Michaelis De Vasconcellos, S.; Bratschitsch, R. Strain Control of Exciton-Phonon Coupling in Atomically Thin Semiconductors. *Nano Lett.* **2018**, *18* (3), 1751–1757.
- (10) Rogers, J. A.; Someya, T.; Huang, Y. Materials and Mechanics for Stretchable Electronics. *Science* **2010**, *327*, 1603–1607.
- (11) Kang, P.; Wang, M. C.; Knapp, P. M.; Nam, S. W. Crumpled Graphene Photodetector with Enhanced, Strain-Tunable, and Wavelength-Selective Photoresponsivity. *Adv. Mater.* **2016**, *28* (23), 4639–4645.
- (12) Blees, M. K.; Barnard, A. W.; Rose, P. A.; Roberts, S. P.; McGill, K. L.; Huang, P. Y.; Ruyack, A. R.; Kevek, J. W.; Kobrin, B.; Muller, D. A.; McEuen, P. L. Graphene Kirigami. *Nature* **2015**, *524* (7564), 204–207.
- (13) Moon, H.; Grosso, G.; Chakraborty, C.; Peng, C.; Taniguchi, T.; Watanabe, K.; Englund, D. Dynamic Exciton Funneling by Local Strain Control in a Monolayer Semiconductor. *Nano Lett.* **2020**, *20* (9), 6791–6797.
- (14) Lee, J.; Yun, S. J.; Seo, C.; Cho, K.; Kim, T. S.; An, G. H.; Kang, K.; Lee, H. S.; Kim, J. Switchable, Tunable, and Directable Exciton Funneling in Periodically Wrinkled WS<sub>2</sub>. *Nano Lett.* **2021**, *21*, 43.
- (15) Feng, J.; Qian, X.; Huang, C. W.; Li, J. Strain-Engineered Artificial Atom as a Broad-Spectrum Solar Energy Funnel. *Nat. Photonics* **2012**, *6* (12), 866–872.
- (16) Song, S.; Keum, D. H.; Cho, S.; Perello, D.; Kim, Y.; Lee, Y. H. Room Temperature Semiconductor-Metal Transition of MoTe<sub>2</sub> Thin Films Engineered by Strain. *Nano Lett.* **2016**, *16* (1), 188–193.
- (17) Luo, Y.; Shepard, G. D.; Ardelean, J. V.; Rhodes, D. A.; Kim, B.; Barmak, K.; Hone, J. C.; Strauf, S. Deterministic Coupling of Site-Controlled Quantum Emitters in Monolayer WSe<sub>2</sub> to Plasmonic Nanocavities. *Nat. Nanotechnol.* **2018**, *13* (12), 1137–1142.
- (18) Rivera, P.; Yu, H.; Seyler, K. L.; Wilson, N. P.; Yao, W.; Xu, X. Interlayer Valley Excitons in Heterobilayers of Transition Metal Dichalcogenides. *Nat. Nanotechnol.* **2018**, *13* (11), 1004–1015.
- (19) Carrascoso, F.; Lin, D. Y.; Frisenda, R.; Castellanos-Gomez, A. Biaxial Strain Tuning of Interlayer Excitons in Bilayer MoS<sub>2</sub>. *J. Phys. Mater.* **2020**, *3*, 3.
- (20) Niehues, I.; Blob, A.; Stiehm, T.; Michaelis De Vasconcellos, S.; Bratschitsch, R. Interlayer Excitons in Bilayer MoS<sub>2</sub> under Uniaxial Tensile Strain. *Nanoscale* **2019**, *11* (27), 12788–12792.
- (21) He, Y.; Yang, Y.; Zhang, Z.; Gong, Y.; Zhou, W.; Hu, Z.; Ye, G.; Zhang, X.; Bianco, E.; Lei, S.; Jin, Z.; Zou, X.; Yang, Y.; Zhang, Y.; Xie, E.; Lou, J.; Yakobson, B.; Vajtai, R.; Li, B.; Ajayan, P. Strain-Induced Electronic Structure Changes in Stacked van Der Waals Heterostructures. *Nano Lett.* **2016**, *16* (5), 3314–3320.
- (22) Pak, S.; Lee, J.; Lee, Y. W.; Jang, A. R.; Ahn, S.; Ma, K. Y.; Cho, Y.; Hong, J.; Lee, S.; Jeong, H. Y.; Im, H.; Shin, H. S.; Morris, S. M.; Cha, S.; Sohn, J. I.; Kim, J. M. Strain-Mediated Interlayer Coupling Effects on the Excitonic Behaviors in an Epitaxially Grown MoS<sub>2</sub>/WS<sub>2</sub> van Der Waals Heterobilayer. *Nano Lett.* **2017**, *17* (9), 5634–5640.
- (23) Huang, S.; Zhang, G.; Fan, F.; Song, C.; Wang, F.; Xing, Q.; Wang, C.; Wu, H.; Yan, H. Strain-Tunable van Der Waals Interactions in Few-Layer Black Phosphorus. *Nat. Commun.* **2019**, *10* (1), 1–7.
- (24) Kunstmann, J.; Mooshammer, F.; Nagler, P.; Chaves, A.; Stein, F.; Paradiso, N.; Plechinger, G.; Strunk, C.; Schüller, C.; Seifert, G.; Reichman, D. R.; Korn, T. Momentum-Space Indirect Interlayer Excitons in Transition-Metal Dichalcogenide van Der Waals Heterostructures. *Nat. Phys.* **2018**, *14* (8), 801–805.
- (25) Unuchek, D.; Ciarrocchi, A.; Avsar, A.; Watanabe, K.; Taniguchi, T.; Kis, A. Room-Temperature Electrical Control of Exciton Flux in a van Der Waals Heterostructure. *Nature* **2018**, *560* (7718), 340–344.
- (26) Chiu, M. H.; Li, M. Y.; Zhang, W.; Hsu, W. T.; Chang, W. H.; Terrones, M.; Terrones, H.; Li, L. J. Spectroscopic Signatures for Interlayer Coupling in MoS<sub>2</sub>-WSe<sub>2</sub> van Der Waals Stacking. *ACS Nano* **2014**, *8* (9), 9649–9656.
- (27) He, K.; Poole, C.; Mak, K. F.; Shan, J. Experimental Demonstration of Continuous Electronic Structure Tuning via Strain in Atomically Thin MoS<sub>2</sub>. *Nano Lett.* **2013**, *13* (6), 2931–2936.
- (28) Aslan, O. B.; Deng, M.; Heinz, T. F. Strain Tuning of Excitons in Monolayer WSe<sub>2</sub>. *Phys. Rev. B: Condens. Matter Mater. Phys.* **2018**, *98* (11), 115308.
- (29) Conley, H. J.; Wang, B.; Ziegler, J. I.; Haglund, R. F.; Pantelides, S. T.; Bolotin, K. I. Bandgap Engineering of Strained Monolayer and Bilayer MoS<sub>2</sub>. *Nano Lett.* **2013**, *13* (8), 3626–3630.
- (30) Doratotaj, D.; Simpson, J. R.; Yan, J. A. Probing the Uniaxial Strains in MoS<sub>2</sub> Using Polarized Raman Spectroscopy: A First-Principles Study. *Phys. Rev. B: Condens. Matter Mater. Phys.* **2016**, *93* (7), 075401.
- (31) Wang, Y.; Cong, C.; Qiu, C.; Yu, T. Raman Spectroscopy Study of Lattice Vibration and Crystallographic Orientation of Monolayer MoS<sub>2</sub> under Uniaxial Strain. *Small* **2013**, *9* (17), 2857–2861.
- (32) Liang, F.; Xu, H.; Wu, X.; Wang, C.; Luo, C.; Zhang, J. Raman Spectroscopy Characterization of Two-Dimensional Materials. *Chin. Phys. B* **2018**, *27* (3), 037802.
- (33) Liu, K.; Zhang, L.; Cao, T.; Jin, C.; Qiu, D.; Zhou, Q.; Zettl, A.; Yang, P.; Louie, S. G.; Wang, F. Evolution of Interlayer Coupling in Twisted Molybdenum Disulfide Bilayers. *Nat. Commun.* **2014**, *5*, 1–6.
- (34) Debnath, R.; Maity, I.; Biswas, R.; Raghunathan, V.; Jain, M.; Ghosh, A. Evolution of High-Frequency Raman Modes and Their Doping Dependence in Twisted Bilayer MoS<sub>2</sub>. *Nanoscale* **2020**, *12* (33), 17272–17280.
- (35) Zhang, X.; Qiao, X. F.; Shi, W.; Wu, J. B.; Jiang, D. S.; Tan, P. H. Phonon and Raman Scattering of Two-Dimensional Transition Metal Dichalcogenides from Monolayer, Multilayer to Bulk Material. *Chem. Soc. Rev.* **2015**, *44* (9), 2757–2785.
- (36) Placidi, M.; Dimitrievska, M.; Izquierdo-Roca, V.; Fontané, X.; Castellanos-Gomez, A.; Pérez-Tomás, A.; Mestres, N.; Espindola-Rodríguez, M.; López-Marino, S.; Neuschitzer, M.; Bermudez, V.; Yaremko, A.; Pérez-Rodríguez, A. Multiwavelength Excitation Raman Scattering Analysis of Bulk and Two-Dimensional MoS<sub>2</sub>: Vibrational Properties of Atomically Thin MoS<sub>2</sub> Layers. *2D Mater.* **2015**, *2* (3), 035006.

- (37) Lee, C.; Yan, H.; Brus, L. E.; Heinz, T. F.; Hone, J.; Ryu, S. Anomalous Lattice Vibrations of Single- and Few-Layer MoS<sub>2</sub>. *ACS Nano* **2010**, *4* (5), 2695–2700.
- (38) Perdew, J. P.; Burke, K.; Ernzerhof, M. Generalized Gradient Approximation Made Simple. *Phys. Rev. Lett.* **1996**, *77* (18), 3865–3868.
- (39) Dong, L.; Namburu, R. R.; O'Regan, T. P.; Dubey, M.; Dongare, A. M. Theoretical Study on Strain-Induced Variations in Electronic Properties of Monolayer MoS<sub>2</sub>. *J. Mater. Sci.* **2014**, *49* (19), 6762–6771.
- (40) Grimme, S.; Antony, J.; Ehrlich, S.; Krieg, H. A Consistent and Accurate Ab Initio Parametrization of Density Functional Dispersion Correction (DFT-D) for the 94 Elements H-Pu. *J. Chem. Phys.* **2010**, *132* (15), 154104.
- (41) Grimme, S.; Ehrlich, S.; Goerigk, L. Effect of the Damping Function in Dispersion Corrected Density Functional Theory. *J. Comput. Chem.* **2011**, *32*, 1456–1465.
- (42) Chang, C. H.; Fan, X.; Lin, S. H.; Kuo, J. L. Orbital Analysis of Electronic Structure and Phonon Dispersion in MoS<sub>2</sub>, MoSe<sub>2</sub>, WS<sub>2</sub>, and WSe<sub>2</sub> Monolayers under Strain. *Phys. Rev. B: Condens. Matter Mater. Phys.* **2013**, *88* (19), 1–9.
- (43) Waters, D.; Nie, Y.; Lupke, F.; Pan, Y.; Folsch, S.; Lin, Y.-C.; Jariwala, B.; Zhang, K.; Wang, C.; Lv, H.; Cho, K.; Xiao, D.; Robinson, J. A.; Feenstra, R. M. Flat Bands and Mechanical Deformation Effects in the Moiré Superlattice of MoS<sub>2</sub>-WSe<sub>2</sub> Heterobilayers. *ACS Nano* **2020**, *14* (6), 7564–7573.
- (44) Zhang, C.; Chuu, C. P.; Ren, X.; Li, M. Y.; Li, L. J.; Jin, C.; Chou, M. Y.; Shih, C. K. Interlayer Couplings, Moiré Patterns, and 2D Electronic Superlattices in MoS<sub>2</sub>/WSe<sub>2</sub> Hetero-Bilayers. *Sci. Adv.* **2017**, *3* (1), 1–8.
- (45) Chiu, M.; Zhang, C.; Shiu, H.; Chuu, C.; Chen, C.; Chang, C. S.; Chen, C.; Chou, M.; Shih, C.; Li, L. Determination of Band Alignment in the Single-Layer MoS<sub>2</sub>/WSe<sub>2</sub> Heterojunction. *Nat. Commun.* **2015**, *6*, 1–6.
- (46) Liu, Z.; Amani, M.; Najmaei, S.; Xu, Q.; Zou, X.; Zhou, W.; Yu, T.; Qiu, C.; Birdwell, A. G.; Crowne, F. J.; Vajtai, R.; Yakobson, B. I.; Xia, Z.; Dubey, M.; Ajayan, P. M.; Lou, J. Strain and Structure Heterogeneity in MoS<sub>2</sub> Atomic Layers Grown by Chemical Vapour Deposition. *Nat. Commun.* **2014**, *5*, 5.
- (47) Kresse, G.; Hafner, J. Ab Initio Molecular Dynamics for Liquid Metals. *Phys. Rev. B: Condens. Matter Mater. Phys.* **1993**, *47* (1), 558–561.